

Electrically tunable dipolar polaritons with giant nonlinearity in a homobilayer microcavity

Baixu Xiang^{1, #}, Yubin Wang^{1, #}, Guihan Wen^{1, #}, Yitong Li¹, Hao Wen¹, Zengde She², Haiyun Liu³, Kenji Watanabe⁴, Takashi Taniguchi⁵, Timothy C. H. Liew⁶, Zhiyuan Sun¹, Qihua Xiong^{1,3,7 *}

¹ State Key Laboratory of Low-Dimensional Quantum Physics and Department of Physics, Tsinghua University, Beijing, China.

² Department of Physics, University of Washington, Seattle, USA.

³ Beijing Academy of Quantum Information Sciences, Beijing, China.

⁴ Research Center for Electronic and Optical Materials, National Institute for Materials Science, Tsukuba, Japan.

⁵ Research Center for Materials Nano architectonics, National Institute for Materials Science, Tsukuba, Japan.

⁶ Division of Physics and Applied Physics, School of Physical and Mathematical Sciences, Nanyang Technological University, Singapore.

⁷ Frontier Science Center for Quantum Information, Beijing, China.

These authors contributed equally: Baixu Xiang, Yubin Wang, Guihan Wen.

To whom correspondence should be addressed. Email: qihua_xiong@tsinghua.edu.cn.

Abstract

Active control over strong optical nonlinearity in solid-state systems is central to unlocking exotic many-body phenomena and scalable photonic devices. While exciton-polaritons in transition metal dichalcogenides (TMDs) offer a promising platform, their practical utility is often impeded by fixed interaction parameters and an intrinsic trade-off between nonlinearity and oscillator strength. Here, we report electrically tunable dipolar polaritons in a dual-gated bilayer MoS₂ microcavity, demonstrating *in situ* reshaping of the dispersion and modulation of the light-matter coupling strength *via* the quantum-confined Stark effect. Crucially, this architecture enables a giant polariton-polariton interaction strength tunable by a factor of seven. This nonlinearity enhancement arises from a synergistic interplay, in which the electric field amplifies the microscopic dipolar repulsion while simultaneously optimizing the macroscopic excitonic Hopfield coefficient. Furthermore, electrostatic doping serves as an independent control knob to switch the system between strong and weak coupling regimes. Our findings bridge the gap between strong optical coupling and giant dipolar nonlinearities, establishing the TMD homobilayer as a versatile platform for engineering programmable correlated many-body states on a chip.

Introduction

Realizing strong, electrically tunable photon-photon interactions in solid-state systems is a long-standing goal for quantum photonics, underpinning the development of programmable simulators and logic gates^{1,2}. Exciton-polaritons—bosonic quasiparticles formed by the strong coupling between cavity photons and material excitons—offer a compelling platform for this pursuit³. By inheriting the small effective mass of their photon component and the strong nonlinear interactions of their excitonic counterpart, polaritons can manifest macroscopic collective phenomena, including low-threshold lasing⁴, polariton condensation^{5–8}, and superfluidity⁹.

Monolayer transition metal dichalcogenides (TMDs) have recently emerged as

appealing systems for studying exciton-polaritons, featuring tightly bound intralayer excitons with large oscillator strength¹⁰⁻¹³. However, their practical utility is often hindered by weak, short-range interactions stemming from the small Bohr radius of intralayer excitons and their limited lifetimes¹⁴⁻¹⁶. Various strategies, including the utilization of trions¹⁷, polarons¹⁸, biexcitons¹⁹, Rydberg states²⁰, and the confinement potentials in traps²¹ or moiré superlattices²², have been employed to enhance nonlinearity. Yet, a critical bottleneck remains: active control over the polariton properties is typically limited once microcavity devices are fabricated²³. For the next generation of integrated polaritonic devices, tunable and reconfigurable nonlinear interactions are highly desirable. Although electrostatic doping has been widely used to modulate intralayer polaritons^{17,18,24,25}, integrating *in situ* electrical field control is essential to transcend from observing passive phenomena to engineering programmable photonic circuits, as previously demonstrated in III-V quantum well systems²⁶⁻²⁹.

To simultaneously address the limitations of weak, short-range interactions and restricted tunability inherent to intralayer excitons, interlayer excitons (IEs) in bilayer TMDs offer a promising platform by separating electrons and holes into adjacent layers³⁰. This charge separation creates permanent out-of-plane electric dipoles, exhibiting long-range interactions^{31,32}, extended lifetimes³³, and high electrical tunability^{34,35}. Nevertheless, IEs in TMD heterobilayers usually suffer from weak oscillator strength, which is typically two orders of magnitude lower than that of intralayer excitons due to spatial electron-hole separation, precluding the realization of dipolar polaritons in the robust strong coupling regime³⁶⁻³⁸.

A distinct solution to overcome this oscillator strength bottleneck is offered by the naturally stacked 2H-MoS₂ homobilayer, where two identical monolayers are rotated 180° relative to each other, retaining an inversion symmetry (Fig.1a). In this system, the hole is delocalized across the layers mediated by coherent tunneling, resulting in the hybridization of the momentum-direct intralayer B exciton and momentum-indirect IE (Fig.1b)³⁹⁻⁴¹. Consequently, unlike the heterobilayer counterparts, IEs in MoS₂ homobilayer exhibit both strong oscillator strength and electric-field tunability. While

recent studies have demonstrated the giant Stark effect in bare IEs^{39–43}, and the formation of static dipolar polaritons^{44–46}, the rich physics of electrically controlled dipolar polaritons remains largely unexplored. Specifically, the ability to dynamically modulate the fundamental Hamiltonian parameters—such as the light-matter coupling strength and the interaction coefficient—has not been realized in the two-dimensional semiconductor microcavities.

Here, we address these challenges by integrating a dual-gated bilayer MoS₂ device into a planar optical microcavity, reporting the first realization of electrically tunable dipolar polaritons in an atomically thin semiconductor system. Unlike previous static demonstrations, our device architecture allows us to continuously reconfigure the polariton band structure and tune the light-matter coupling strength *via* the quantum-confined Stark effect. This dynamic control enables us to access a regime of giant nonlinearity, where the polariton-polariton interaction strength is enhanced by seven-fold compared to the zero-field baseline. This giant nonlinearity stems from a constructive interplay between the enhanced microscopic dipolar repulsion and the optimization of the macroscopic excitonic Hopfield coefficient. Furthermore, by exploiting carrier density as an additional degree of freedom, we implement an all-electrical control that switches between weak and strong coupling regimes. This extensive electrical control over dipolar polaritons paves the way for defining reconfigurable potential landscapes without lithography, bringing the elusive regime of polariton blockade within reach and enabling the development of deterministic quantum logic devices.

Results

Intrinsic excitonic landscape and electrical tunability of bilayer MoS₂.

In our experiment, we encapsulate a natural bilayer MoS₂ within hexagonal boron nitride (hBN) flakes and integrate the bilayer sample into a dual-gate structure, as schematically illustrated in Fig. 1c. Monolayer graphene serves as the top and bottom

gate electrodes, specifically selected for high transparency to minimize optical absorption losses in subsequent cavity integration steps⁴⁷. The bilayer MoS₂ is grounded by a few-layer graphite electrode. This device architecture enables independent control over the out-of-plane electric field E_z and the electrostatic doping density n within the sample (see Supplementary Note 1)⁴⁸, where n is the carrier density. Figure 1d shows an optical micrograph of a typical device. For the cavity integration, this heterostructure serves as the active medium within a planar microcavity, composed of a 9-period distributed Bragg reflector (DBR) bottom mirror and a 50 nm silver top mirror (see Methods for more fabrication details).

We first characterize the intrinsic excitonic landscape of the bilayer MoS₂ by performing reflectivity spectroscopy at 9 K in a half-cavity configuration (prior to top-mirror transfer). At zero electric field ($E_z = 0$ V/nm, black curve in Fig. 1e), the spectrum reveals three dominant resonances corresponding to the ground-state A exciton (A_{1s}) at 1.929 eV, the B exciton at 2.106 eV, and the IE at 1.996 eV that retains a substantial oscillator strength (~35% of the A_{1s} resonance), respectively. Upon applying a vertical electric field of $E_z = 0.03$ V/nm (red curve in Fig. 1e), the single IE resonance splits into two distinct branches, labeled as IE_L (low-energy exciton) and IE_H (high-energy exciton). These two branches correspond to IEs with permanent out-of-plane electric dipoles oriented antiparallel to each other⁴⁹. The evolution of these resonances is mapped in Fig. 1f, where the IEs manifest a large Stark splitting with a characteristic “X”-shaped field dependence. In contrast, the intralayer A_{1s} and B exciton remain largely insensitive to the field, confirming the dominant interlayer character of the IE state^{39,41}.

From the linear Stark shift, we extract the effective permanent electric dipole moments p_{eff} to be around 0.40 e·nm for both IE_L and IE_H (see Supplementary Note 2). By benchmarking the measured effective dipole moment p_{eff} against the theoretical limit of a pure interlayer state, $p_0 \approx 0.65$ e·nm (determined by the geometric layer separation $d_0 \approx 0.65$ nm)³⁵, we estimate the interlayer component weight $|C_{\text{IE}}|^2 = p_{\text{eff}}/p_0 \approx 0.61$. This result indicates that the observed state is a

hybridized admixture of the pure IE and the intralayer B exciton, an assignment consistent with previous theoretical and experimental studies that attribute this mixing to coherent hole tunneling^{39–41}. This tunneling-mediated intralayer contribution endows the dipolar IEs with robust oscillator strength, making them ideal candidates for strong light-matter coupling. Additionally, we observe a weak resonance near 2.072 eV, exhibiting a perceptible Stark shift parallel to the ground state (Fig. 1f), which we attribute to the first excited Rydberg state of the IEs, labeled as IE_{2s} (see Supplementary Note 3).

We further explore the independent knob of electrostatic doping by varying the carrier density n at zero electric field (Fig. 1g). The system exhibits a pronounced asymmetry between electron and hole doping. Upon electron doping ($n > 0$), the neutral A_{1s} resonance evolves into a blue-shifted and broadened repulsive polaron (RP) branch, which rapidly loses oscillator strength due to phase-space filling and exchange interactions with the Fermi sea^{18,50}. Concurrently, the spectral weight is transferred to a redshifted attractive polaron (AP) branch (conventionally termed the trion, A[−]), which emerges at lower energies^{24,51}. Significantly, the IE resonance is also suppressed as the intralayer RP loses its spectral weight, eventually vanishing at higher carrier densities. In stark contrast, under hole doping ($n < 0$), both the A_{1s} and IE maintain their robust oscillator strength across the entire probed density range. We attribute this pronounced asymmetry of the IE to the specific band structure of bilayer MoS₂, where the valence band maximum is located at the Γ point of the Brillouin zone—approximately 400 meV higher in energy than the local maximum at the K point, as confirmed by angle-resolved photoemission spectroscopy and theoretical calculation in previous studies^{52,53}. Quantitative estimation indicates that within our experimental doping range ($|n| \leq 6 \times 10^{11} \text{ cm}^{-2}$), the induced downward shift of the Fermi level is merely ~ 2.4 meV (see Supplementary Note 4 for estimation details), which is insufficient to overcome this large Γ - K valence band offset. This energy barrier ensures that the injected holes populate the Γ valley, remaining kinetically decoupled from the K -valley optical transitions. As a result, the large momentum mismatch effectively suppresses Pauli

blocking and exchange interactions, preserving the oscillator strength of excitonic states. In contrast, the conduction band minimum is located at the K valleys, meaning injected electrons directly occupy the phase space required for the K -valley optical transitions^{54,55}. This leads to efficient Pauli blocking and screening, rapidly suppressing the excitonic resonances observed in the electron-doped regime. Collectively, the comprehensive control over energy, dipole orientation, and the existence of hybrid excitons establishes the bilayer MoS₂ device as an exceptionally versatile platform for investigating tunable strong light-matter coupling physics.

Electrically tunable nonlinearity and ultrafast dynamics in bilayer MoS₂.

Having established the steady-state electrical tunability, we then employ ultrafast pump-probe spectroscopy to investigate the nonlinear interactions and dynamics of the hybrid IEs. A narrow-band pump pulse (FWHM of 50 meV) centered at 2.070 eV, resonant with the B exciton transitions, is used to excite the system, while a delayed broadband supercontinuum pulse probes the transient response of the bilayer MoS₂ (see Methods for more details). Figure 2a and 2b display the pump fluence-dependent reflectivity spectra for IE_L at a fixed delay of 200 fs (zero time is defined in Methods). At $E_z = 0$ V/nm (Fig. 2a), increasing pump fluence induces a small blueshift of IE_L (up to \sim 1.4 meV), accompanied by noticeable peak broadening and bleaching. Strikingly, at $E_z = 0.07$ V/nm (Fig. 2b), the resonance exhibits a pronounced density-dependent blueshift (up to \sim 5.2 meV). We quantified this nonlinearity by extracting the energy shift of IE_L ΔE_L as a function of the exciton density n_{exc} by Lorentzian lineshape analysis. As shown in Fig. 2c, the magnitude of blueshift exhibits a pronounced dependence on the applied field. The effective exciton-exciton interaction strength g_{exc} , defined by the slope $\Delta E_L = g_{\text{exc}}n_{\text{exc}}$ in the low-density regime, increases monotonically from 0.29 to 1.81 $\mu\text{eV}\cdot\mu\text{m}^2$ as the field is swept (see Supplementary Note 5 for more quantification details). This corresponds to a six-fold continuous increase in interaction strength over the investigated field range.

To elucidate the microscopic origin of this giant nonlinearity enhancement, we first examine how the electric field modifies the exciton wavefunction. As established above, the zero-field IE is a hybrid state. Applying an electric field shifts the energy of the IEs relative to the intralayer B exciton *via* the Stark effect, as schematically shown in Fig. 2d and 2e. For the IE_L branch (Fig. 2d), the field increases the energy offset from the B exciton. This large energy offset effectively suppresses the resonant hybridization mediated by the hole tunneling strength J (see Supplementary Note 6), forcing the exciton to acquire a more pristine interlayer character. As a result, we observe two concurrent signatures of de-hybridization: a reduction in oscillator strength, quantified by fitting the spectra in Fig. 1f (see Supplementary Note 7) and an increase in the effective permanent dipole moment from $0.40 \text{ e}\cdot\text{nm}$ to $0.48 \text{ e}\cdot\text{nm}$ for IE_L , determined by fitting the Stark shift with a quadratic polynomial (see Supplementary Note 2). Quantitatively, this corresponds to an increase in the interlayer component weight $|C_{IE}|^2$ from approximately 61% to 72%. Nevertheless, the increased permanent dipole leads to a weak enhancement of dipole-dipole repulsion ($g_{dd} \propto p_{\text{eff}}^2 \propto |C_{IE}|^4$) (see Supplementary Note 8 for the derivation) by a factor of ~ 1.4 , far from enough to explain the six-fold enhancement for the bare IE_L system.

To better explain the substantial modulation of ΔE_L , we write it as the Hartree shift:

$$\Delta E_L = g_{LL}n_L + g_{LH}n_H$$

Where n_L (n_H) denotes the population density for the lower (higher) energy IE, g_{LL} is the interaction strength between two IE_L , and g_{LH} is that between a IE_L and a IE_H . Assuming the interaction comes only from the dipolar interactions, the intraspecies repulsion scales as $g_{LL} \propto p_L^2 > 0$, while the interspecies attraction scales as $g_{LH} \propto p_L p_H < 0$ (see Supplementary Note 8). At zero electric field, the two interlayer branches are energetically degenerate. In this regime, the exciton population is shared between the two branches ($n_L \approx n_H$). The repulsive interaction within the same branch ($g_{LL}n_L$) is strongly compensated by the attractive interaction between opposite dipoles

($g_{\text{LH}} n_{\text{H}}$). This compensation leads to the suppressed net nonlinearity, consistent with the small blueshift observed at $E_z = 0$ V/nm. The residual small blueshift likely originates from the short-range exchange interactions or local symmetry breaking due to structural disorder^{44,45}. At nonzero electric fields, the colossal Stark splitting lifts the degeneracy. The excitons efficiently relax to the energetic ground state (IE_L), leading to a highly polarized population distribution where n_{L} is much larger than n_{H} . This population imbalance effectively reduces the compensation effect mediated by the attractive g_{LH} term. Therefore, the giant nonlinearity is attributed to a combined effect: the field-induced enhancement of individual dipole moment, and the field-selection of the repulsive species as the dominant population. Ideally, for fully aligned dipole excitons, the interaction strength is predicted to reach ~ 1.8 $\mu\text{eV}\cdot\mu\text{m}^2$ (see Methods for more estimation details)⁵⁶. Our measured value of 1.81 $\mu\text{eV}\cdot\mu\text{m}^2$ approaches this theoretical limit, indicating that the applied electric field efficiently suppresses the compensation effect and drives the system toward a strongly enhanced interacting regime.

Conversely, for the IE_H branch (Fig. 2e), the electric field reduces the energy offset between IE_H and B exciton, thereby enhancing the tunneling-mediated hybridization (J). This leads to a stronger hybridization of the intralayer B component. Thus, the IE_H inherits large oscillator strength from the bright B exciton (see Supplementary Note 7), while its dipolar character is simultaneously diminished. This complex composition results in a competition between the enhanced short-range exchange interaction from the B component and the suppressed long-range dipolar interaction, leading to the observed non-monotonic behavior and smaller blue shift (see Supplementary Note 9).

This microscopic reconfiguration also profoundly reshapes the ultrafast carrier dynamics. Figure 2f compares the relaxation of the interaction-induced blueshift for IE_L under varying electric fields. We observe that higher electric fields not only enhance the initial blueshift magnitude but also significantly prolong the recovery time. This trend is consistent with the reduced electron-hole overlap integral, which suppresses the radiative recombination rate and extends the lifetime of the interacting dipolar state.

Our findings unveil a direct and versatile control of many-body interactions. While the strategy of electrically tuning many-body interactions has been established in theoretical frameworks⁵⁷⁻⁵⁹ and shown experimentally in WSe₂ homobilayers or type-II heterostructures^{31,35,59,34}, these systems are typically constrained by momentum-indirect dark excitons with small oscillator strengths. Therefore, probing their nonlinear interactions often relies on spatially resolved transport or diffusion measurements. In stark contrast, the unique hybrid IEs in the naturally bilayer MoS₂ investigated here possess a large oscillator strength comparable to that of intralayer excitons. This unique feature allows us to directly probe the pronounced interaction-induced energy shifts using transient reflectivity spectroscopy, distinguishing our work from previous transport-centric studies by enabling the direct optical manipulation and readout of dipolar many-body physics.

Electrically reconfigurable strong coupling in a planar microcavity.

We next integrate the dual-gated heterostructure into a planar microcavity to investigate the electrical control of strongly coupled light-matter states. The microcavity is formed by transferring a 50 nm Ag top mirror, featuring a PMMA spacer designed to position the bilayer MoS₂ precisely at the optical field antinode. The fundamental cavity mode is set to a negative detuning of ~ 47 meV relative to the hybrid IE at $k_{\parallel}/k_0 = 0$, where k_{\parallel} and k_0 denote the in-plane and free-space wave vectors, respectively (see Supplementary Note 10).

Angle-resolved reflectivity spectroscopy at $E_z = 0$ V/nm (Fig. 3a) reveals four distinct polariton branches, which is an unambiguous signature of the multimode strong coupling regime. The single cavity mode is simultaneously coupled to the intralayer A exciton, IE, and intralayer B exciton^{44,45}, respectively. By fitting the dispersion with a four-coupled-oscillator model (see Supplementary Note 11), we extract the Rabi splittings, yielding $\Omega_A = 56.2$ meV, $\Omega_{IE} = 30.4$ meV, and $\Omega_B = 53.6$ meV, respectively. Importantly, these values satisfy the strong coupling criterion $2\Omega >$

$\gamma_{\text{cav}} + \gamma_{\text{exc}}$, where γ_{cav} and γ_{exc} are the cavity and exciton linewidths, respectively^{10,60}. This confirms that all excitonic species, particularly the optically active hybrid IEs, are strongly coupled to the cavity mode (see Supplementary Note 12).

Leveraging the Stark effect, we dynamically reconfigure the polaritonic band structure. As the electric field splits the bare IE resonance into dipolar IE_L and IE_H branches, the polariton dispersion transforms from a four-branch to a five-branch system (Fig. 3b). The detailed evolution of these dispersion branches is provided in Supplementary Note 13. To further visualize this electrical control, we extract the reflectivity at $k_{\parallel}/k_0 = 0.33$, where the cavity mode and hybrid energy are crossing and plot as a function of the applied electric field as shown in Fig. 3c. The polariton branches associated with the IE resonance shift continuously and symmetrically, reflecting the underlying Stark effect. A five-coupled-oscillator model accurately reproduces the full field-dependent dispersion (see Supplementary Note 11). The extracted energies of the IE_L and IE_H are in excellent agreement with the values measured independently in the half-cavity configuration (see Supplementary Note 14 and Supplementary Figure S1), confirming the validity of our model. Notably, our analysis reveals that the light-matter coupling strength V itself is highly tunable *via* the electric field. As extracted from the model and plotted in Fig. 3d, the coupling strength for IE_H branches V_{IE_H} nearly doubles as the electric field sweeps from 0 to 0.08 V/nm. This enhancement stems from the field-driven hybridization. As the field tunes the IE_H closer to the bright intralayer B exciton, it acquires large oscillator strength through hybridization, as shown in Fig. 1f and Supplementary Fig. S4. In contrast, the effective coupling strength of the lower branch V_{IE_L} maintains a robust magnitude (~ 12 meV) throughout the tuning range, despite the reduction in the bare oscillator strength (see Supplementary Fig. S4).

Additionally, we demonstrate that strong coupling can be selectively quenched *via* electrostatic doping (see Supplementary Note 15 for the full spectral evolution). Figure 3e maps the zero-detuning reflectivity as a function of doping density. Consistent

with our half-cavity device measurements (Fig. 1g), electron-doping quenches the oscillator strength of the IE resonances due to Pauli blocking and screening⁶¹. Therefore, the extracted coupling strength V_{IE} decreases continuously with electron density (Fig. 3f), driving the system from the strong coupling into the weak coupling regime (see Supplementary Note 16 for more details). This effect is absent under hole doping, realizing a polarity-dependent switch for polariton states^{61,62}. Such electrical switching between coupling regimes offers a mechanism for active polariton gating and routing, essential for constructing integrated logic circuits.

Electrical tuning of the nonlinearity of the dipolar polaritons

Finally, we investigate the nonlinear interactions of these electrically reconfigurable polaritons using angle-resolved ultrafast pump-probe spectroscopy⁶³. We utilized the same pump-probe configuration as in the bare exciton study, resonantly pumping the B exciton transitions while probing the broadband transient reflectivity (see Methods and Supplementary Note 17). Figures 4a and 4b present the resonant reflectivity spectra of the polariton branches at $E_z = 0$ V/nm and at a finite field $E_z = 0.04$ V/nm, respectively. In both regimes, increasing pump fluences induces a clear energy blueshift of the polariton resonances—a signature of repulsive polariton-polariton interactions enhanced by the dipolar character of the excitonic component.

To quantify the electrical control over the polariton nonlinearity, we extract the energy shift of the lower polariton branch (LPB) associated with the IE_L at zero-detuning ($k_{||}/k_0 = 0.33$) as a function of polariton density (Fig. 4c). The data is presented on a logarithmic density scale to visualize the broad dynamic range, while the linear-scale inset highlights the steep rise in the low-density regime. This rapid initial blueshift implies a giant interaction strength before the onset of saturation. At higher densities, the shift rapidly saturates. We attribute this to the phase space filling effect, which reduces the Rabi splitting and counteracts the interaction-induced blueshift, consistent with previous reports on dipolar polaritons in bilayer MoS₂⁴⁴.

Given this saturation behavior, we define the polariton-polariton interaction strength g_{LP} as the ratio of the shift to the density. Using this metric, we find that g_{LP} exhibits a remarkable dependence on the electric field. As plotted in Fig. 4d, g_{LP} increases from 0.09 to 0.60 $\mu\text{eV}\cdot\mu\text{m}^2$ in the low-density limit with the application of the electric field, representing a nearly seven-fold enhancement over the applied range. Given the rapid saturation due to screening phase-space filling effect (Fig. 4c, inset), the intrinsic nonlinearity in the dilute limit is expected to be significantly larger, potentially comparable to the giant interaction strengths reported in tightly confined moiré polariton systems²². However, distinct from those static architectures, our platform offers the unique advantage of wide-range *in situ* electrical tunability^{44,45}.

This macroscopic enhancement surpasses the scaling observed for bare excitons alone (compare Fig. 4d with Fig. 2c). We trace this amplification to a synergistic dual mechanism. Firstly, the electric field enhances the microscopic dipolar repulsion g_{exc} , resulting from the field-induced population imbalance where excitons preferentially occupy the strongly dipolar lower branch ($n_L \gg n_H$) and the increased permanent dipole moment, as discussed in the previous section. Secondly, and unique to the cavity system, the electric field dynamically optimizes the polariton composition. The Stark-induced redshift of the exciton energy reduces the exciton-cavity detuning, thereby increasing the excitonic Hopfield coefficient ($|X|^2$) (see Supplementary Note 18). Crucially, since the effective polariton-polariton interaction scales with the fourth power of this excitonic fraction ($g_{LP} \approx |X|^4 g_{exc}$), the field-driven increase in $|X|^2$ acts as a powerful lever to amplify the nonlinear interaction.

Consequently, the giant seven-fold enhancement of g_{LP} is not merely a reproduction of the excitonic behavior, but the combined result of simultaneously boosting the microscopic repulsion and maximizing the macroscopic excitonic participation. By enabling a seven-fold modulation of the nonlinearity within a single device, this work overcomes the limitations of static moiré or monolayer systems, opening new avenues for programmable quantum simulators where interaction parameters can be dynamically reconfigured on demand.

Conclusion

In summary, we have developed a versatile platform for the active electrical control of strongly correlated many-body states, realizing widely tunable dipolar polaritons in an atomically thin semiconductor system. By integrating a high-quality, dual-gated bilayer MoS₂ heterostructure into a planar microcavity, we successfully bridge the gap between the giant nonlinearity of interlayer states and the robust optical coupling of intralayer excitons. Uniquely, our device enables the simultaneous *in situ* modulation of both the light-matter coupling strength and the nonlinear interaction coefficient, unlocking a wide phase space of the polariton Hamiltonian within a single, monolithically integrated device. We identify that this capability is underpinned by a constructive interplay between microscopic and macroscopic tuning mechanisms: the vertical electric field not only amplifies the microscopic dipolar repulsion but also dynamically optimizes the macroscopic excitonic Hopfield coefficient. This synergistic control results in a seven-fold enhancement of the polariton nonlinearity. Furthermore, electrostatic doping acts as an independent transistor-like switch that reversibly toggles the system between strong and weak coupling regimes, providing an efficient all-electrical mechanism to extinguish the polaritonic state on demand.

Our work position dipolar polaritons based on TMD homobilayers as premier candidates for realizing programmable quantum simulators and integrated nonlinear photonic circuits. This electrically reconfigurable platform underpins future efforts to observe polariton blockade and explore quantum sensing²⁸, marking a significant step toward engineered lattices for practical solid-state quantum technologies^{64,65}.

References

1. Amo, A. & Bloch, J. Exciton-polaritons in lattices: A non-linear photonic simulator. *Comptes Rendus Phys.* **17**, 934–945 (2016).
2. Ballarini, D. *et al.* All-optical polariton transistor. *Nat. Commun.* **4**, 1778 (2013).
3. Sanvitto, D. & Kéna-Cohen, S. The road towards polaritonic devices. *Nat. Mater.* **15**, 1061–1073 (2016).
4. Su, R. *et al.* Room-temperature polariton lasing in all-Inorganic perovskite nanoplatelets. *Nano Lett.* **17**, 3982–3988 (2017).
5. Kasprzak, J. *et al.* Bose–Einstein condensation of exciton polaritons. *Nature* **443**, 409–414 (2006).
6. Deng, H., Weihs, G., Santori, C., Bloch, J. & Yamamoto, Y. Condensation of semiconductor microcavity exciton polaritons. *Science* **298**, 199–202 (2002).
7. Anton-Solanas, C. *et al.* Bosonic condensation of exciton–polaritons in an atomically thin crystal. *Nat. Mater.* **20**, 1233–1239 (2021).
8. Zhao, J. *et al.* Ultralow threshold polariton condensate in a monolayer semiconductor microcavity at room temperature. *Nano Lett.* **21**, 3331–3339 (2021).
9. Amo, A. *et al.* Superfluidity of polaritons in semiconductor microcavities. *Nat. Phys.* **5**, 805–810 (2009).
10. Liu, X. *et al.* Strong light–matter coupling in two-dimensional atomic crystals. *Nat. Photonics* **9**, 30–34 (2015).
11. Barachati, F. *et al.* Interacting polariton fluids in a monolayer of tungsten disulfide. *Nat. Nanotechnol.* **13**, 906–909 (2018).
12. Zhao, J. *et al.* Nonlinear polariton parametric emission in an atomically thin semiconductor based microcavity. *Nat. Nanotechnol.* **17**, 396–402 (2022).
13. Sun, Z. *et al.* Optical control of room-temperature valley polaritons. *Nat. Photonics* **11**, 491–496 (2017).
14. Chernikov, A. *et al.* Exciton binding energy and nonhydrogenic Rydberg series in monolayer WS₂. *Phys. Rev. Lett.* **113**, 076802 (2014).
15. Shahnazaryan, V., Iorsh, I., Shelykh, I. A. & Kyriienko, O. Exciton-exciton interaction in transition-metal dichalcogenide monolayers. *Phys. Rev. B* **96**, 115409 (2017).
16. Dufferwiel, S. *et al.* Exciton–polaritons in van der Waals heterostructures embedded in tunable microcavities. *Nat. Commun.* **6**, 8579 (2015).
17. Emmanuele, R. P. A. *et al.* Highly nonlinear trion-polaritons in a monolayer semiconductor. *Nat. Commun.* **11**, 3589 (2020).
18. Tan, L. B. *et al.* Interacting polaron-polaritons. *Phys. Rev. X* **10**, 021011 (2020).
19. Wei, K. *et al.* Charged biexciton polaritons sustaining strong nonlinearity in 2D semiconductor-based nanocavities. *Nat. Commun.* **14**, 5310 (2023).
20. Gu, J. *et al.* Enhanced nonlinear interaction of polaritons via excitonic Rydberg states in monolayer WSe₂. *Nat. Commun.* **12**, 2269 (2021).
21. Shan, H. *et al.* Spatial coherence of room-temperature monolayer WSe₂ exciton-polaritons in a trap. *Nat. Commun.* **12**, 6406 (2021).
22. Zhang, L. *et al.* Van der Waals heterostructure polaritons with moiré-induced nonlinearity. *Nature* **591**, 61–65 (2021).

23. Robert, C. *et al.* Exciton radiative lifetime in transition metal dichalcogenide monolayers. *Phys. Rev. B* **93**, 205423 (2016).
24. Sidler, M. *et al.* Fermi polaron-polaritons in charge-tunable atomically thin semiconductors. *Nat. Phys.* **13**, 255–261 (2017).
25. Smołeński, T. *et al.* Interaction-induced Shubnikov–de Haas oscillations in optical conductivity of monolayer MoSe₂. *Phys. Rev. Lett.* **123**, 097403 (2019).
26. Rosenberg, I. *et al.* Strongly interacting dipolar-polaritons. *Sci. Adv.* **4**, eaat8880 (2018).
27. Tsintzos, S. I. *et al.* Electrical tuning of nonlinearities in exciton-polariton condensates. *Phys. Rev. Lett.* **121**, 037401 (2018).
28. Togan, E., Li, Y., Faelt, S., Wegscheider, W. & Imamoglu, A. Polariton electric-field sensor. *Phys. Rev. Lett.* **125**, 067402 (2020).
29. Liran, D. *et al.* Electrically controlled photonic circuits of field-induced dipolaritons with huge nonlinearities. *Phys. Rev. X* **14**, 031022 (2024).
30. Sun, X., Malic, E. & Lu, Y. Dipolar many-body complexes and their interactions in stacked 2D heterobilayers. *Nat. Rev. Phys.* **6**, 439–454 (2024).
31. Sun, Z. *et al.* Excitonic transport driven by repulsive dipolar interaction in a van der Waals heterostructure. *Nat. Photonics* **16**, 79–85 (2022).
32. Li, W., Lu, X., Dubey, S., Devenica, L. & Srivastava, A. Dipolar interactions between localized interlayer excitons in van der Waals heterostructures. *Nat. Mater.* **19**, 624–629 (2020).
33. Rivera, P. *et al.* Observation of long-lived interlayer excitons in monolayer MoSe₂–WSe₂ heterostructures. *Nat. Commun.* **6**, 6242 (2015).
34. Jauregui, L. A. *et al.* Electrical control of interlayer exciton dynamics in atomically thin heterostructures. *Science* **366**, 870–875 (2019).
35. Tagarelli, F. *et al.* Electrical control of hybrid exciton transport in a van der Waals heterostructure. *Nat. Photonics* **17**, 615–621 (2023).
36. Wilson, N. R. *et al.* Determination of band offsets, hybridization, and exciton binding in 2D semiconductor heterostructures. *Sci. Adv.* **3**, e1601832 (2017).
37. Chen, H. *et al.* Ultrafast formation of interlayer hot excitons in atomically thin MoS₂/WS₂ heterostructures. *Nat. Commun.* **7**, 12512 (2016).
38. Barré, E. *et al.* Optical absorption of interlayer excitons in transition-metal dichalcogenide heterostructures. *Science* **376**, 406–410 (2022).
39. Leisgang, N. *et al.* Giant Stark splitting of an exciton in bilayer MoS₂. *Nat. Nanotechnol.* **15**, 901–907 (2020).
40. Lorchat, E. *et al.* Excitons in bilayer MoS₂ displaying a colossal electric field splitting and tunable magnetic response. *Phys. Rev. Lett.* **126**, 037401 (2021).
41. Peimyoo, N. *et al.* Electrical tuning of optically active interlayer excitons in bilayer MoS₂. *Nat. Nanotechnol.* **16**, 888–893 (2021).
42. Lopriore, E. *et al.* Electrically tunable ultrafast dynamics and interactions of hybrid excitons in a 2D semiconductor bilayer. *Nat. Commun.* **16**, 10710 (2025).
43. Liu, X. *et al.* Optical signatures of interlayer electron coherence in a bilayer semiconductor. *Nat. Phys.* **21**, 1563–1569 (2025).
44. Datta, B. *et al.* Highly nonlinear dipolar exciton-polaritons in bilayer MoS₂. *Nat. Commun.* **13**, 6341 (2022).

45. Louca, C. *et al.* Interspecies exciton interactions lead to enhanced nonlinearity of dipolar excitons and polaritons in MoS₂ homobilayers. *Nat. Commun.* **14**, 3818 (2023).
46. Genco, A. *et al.* Femtosecond switching of strong light-matter interactions in microcavities with two-dimensional semiconductors. *Nat. Commun.* **16**, (2025).
47. Gu, J., Chakraborty, B., Khatoniar, M. & Menon, V. M. A room-temperature polariton light-emitting diode based on monolayer WS₂. *Nat. Nanotechnol.* **14**, 1024–1028 (2019).
48. Wang, Z., Chiu, Y.-H., Honz, K., Mak, K. F. & Shan, J. Electrical tuning of interlayer exciton gases in WSe₂ bilayers. *Nano Lett.* **18**, 137–143 (2018).
49. Feng, S. *et al.* Quadrupolar and dipolar excitons in bilayer 2H-MoSe₂. *Phys. Rev. Lett.* **134**, 166901 (2025).
50. Tan, L. B. *et al.* Bose polaron interactions in a cavity-coupled monolayer semiconductor. *Phys. Rev. X* **13**, 031036 (2023).
51. Xiang, B. *et al.* Chirality-dependent dynamic evolution for trions in monolayer WS₂. *Nano Lett.* **24**, 6592–6600 (2024).
52. Jin, W. *et al.* Direct measurement of the thickness-dependent electronic band structure of MoS₂ using angle-resolved photoemission spectroscopy. *Phys. Rev. Lett.* **111**, 106801 (2013).
53. Yeh, P.-C. *et al.* Direct measurement of the tunable electronic structure of bilayer MoS₂ by Interlayer Twist. *Nano Lett.* **16**, 953–959 (2016).
54. Kormányos, A. *et al.* $k \cdot p$ theory for two-dimensional transition metal dichalcogenide semiconductors. *2D Mater.* **2**, 022001 (2015).
55. Liu, G.-B., Shan, W.-Y., Yao, Y., Yao, W. & Xiao, D. Three-band tight-binding model for monolayers of group-VIB transition metal dichalcogenides. *Phys. Rev. B* **88**, 085433 (2013).
56. Gu, L. *et al.* Giant optical nonlinearity of Fermi polarons in atomically thin semiconductors. *Nat. Photonics* **18**, 816–822 (2024).
57. Erkensten, D., Brem, S., Perea-Causín, R. & Malic, E. Microscopic origin of anomalous interlayer exciton transport in van der Waals heterostructures. *Phys. Rev. Mater.* **6**, 094006 (2022).
58. Erkensten, D., Brem, S. & Malic, E. Exciton-exciton interaction in transition metal dichalcogenide monolayers and van der Waals heterostructures. *Phys. Rev. B* **103**, 045426 (2021).
59. Steinhoff, A. *et al.* Exciton-exciton interactions in Van der Waals heterobilayers. *Phys. Rev. X* **14**, 031025 (2024).
60. Weisbuch, C., Nishioka, M., Ishikawa, A. & Arakawa, Y. Observation of the coupled exciton-photon mode splitting in a semiconductor quantum microcavity. *Phys. Rev. Lett.* **69**, 3314–3317 (1992).
61. Chakraborty, B. *et al.* Control of strong light-matter interaction in monolayer WS₂ through electric field gating. *Nano Lett.* **18**, 6455–6460 (2018).
62. Mondal, A. *et al.* Switching polariton screening in MoS₂ microcavity toward polaritonics. *Sci. Adv.* **11**, eadr7202 (2025).
63. Zhao, J. *et al.* Exciton polariton interactions in Van der Waals superlattices at room temperature. *Nat. Commun.* **14**, 1512 (2023).
64. Muñoz-Matutano, G. *et al.* Emergence of quantum correlations from interacting fibre-

cavity polaritons. *Nat. Mater.* **18**, 213–218 (2019).

65. Delteil, A. *et al.* Towards polariton blockade of confined exciton–polaritons. *Nat. Mater.* **18**, 219–222 (2019).

Methods

Device and microcavity fabrication.

The bottom distributed Bragg reflector (DBR), consisting of 18 alternating layers of titanium dioxide (TiO_2) and silicon dioxide (SiO_2) layers, was deposited on a silicon substrate by electron-beam evaporation. Standard lithography was subsequently used to pattern Cr/Au contacts on the DBR surface to define the gate electrodes.

The heterostructure was assembled using mechanically exfoliated 2H-stacked bilayer MoS_2 , monolayer graphene, and hBN flakes. Monolayer graphene was chosen for the top and bottom gate electrodes to minimize optical absorption, thereby mitigating the degradation of the cavity quality factor. The 2H-stacked bilayer MoS_2 flake, identified and confirmed by its characteristic reflectance and Raman spectra, was encapsulated between hBN flakes with nearly identical thickness (~ 12 nm) serving as the gate dielectrics. The stack was then assembled in a graphene/hBN/bilayer MoS_2 /hBN/graphene sequence using a polycarbonate (PC)-based dry transfer technique, and subsequently transferred onto the DBR substrate, with the graphene gates precisely aligned to the pre-fabricated contacts.

To complete the $\lambda/2$ microcavity, a poly-methyl methacrylate (PMMA) spacer was spin-coated over the heterostructure. Finally, a 50 nm silver film, serving as the top mirror, was transferred onto the PMMA using a polydimethylsiloxane (PDMS, PF-X4, Gel-Pack) stamp-assisted method.

Optical measurements.

Experimental setup. All optical measurements were performed at 9 K using a home-built, angle-resolved confocal spectral setup based on a microscope (Olympus). The sample was mounted in a closed-cycle cryostat (CIA). A $50\times$ objective with a numerical aperture (NA) of 0.7 was used for both sample excitation and signal collection. The signal was dispersed by a Horiba iHR550 spectrometer, equipped with interchangeable 300 and 600 grooves/mm gratings, and detected by a liquid-nitrogen-cooled charge-

coupled device (CCD, Symphony II). For all experiments, gate voltages were supplied by a source meter (Keithley 2614B). The system can be configured to image either the real plane or the Fourier plane of the objective onto the spectrometer entrance slit to acquire real-space or angle-resolved (k-space) spectra, respectively.

Steady-state reflectivity. The device was illuminated with a broadband halogen lamp (Thorlabs OSL2IR). Reflectivity contrast spectra were obtained by normalizing the signal from the device area to a reference spectrum from the substrate.

Transient reflectivity spectroscopy. The ultrafast optical response was investigated using a pump-probe configuration integrated into the confocal system. The light source was a regeneratively amplified Ti: sapphire laser system (Coherent, Astrella) delivering 100 fs pulses at 800 nm with a repetition rate of 5 kHz. The beam was split into pump and probe paths. The pump beam was converted to the desired wavelength using an optical parametric amplifier (OPA, Light Conversion) and spectrally shaped using a bandpass filter (FWHM~50 meV) to ensure selective excitation. The probe beam was a broadband supercontinuum light (480-820 nm) generated in a sapphire crystal, with the time delay controlled by a motorized mechanical delay stage. The pump and probe beams were collinearly focused and spatially overlapped on the sample surface, yielding spot diameters of approximately 3 μm and 2 μm , respectively. Transient reflectivity spectra were recorded as a function of the pump-probe delay, with time zero defined by the temporal overlap of the pulses. For angle-resolved pump-probe spectroscopy, the back focal plane (Fourier plane) of the objective was imaged onto the spectrometer slit, enabling the mapping of transient carrier dynamics in energy-momentum space.

Estimate of the exciton density.

For the fluence-dependent measurements in the half-cavity configuration presented in Fig. 2c, we estimate the exciton density using the relation:

$$n_{\text{exc}} = \frac{P\alpha}{RA_{\text{laser}}E_{\text{pump}}}$$

where P is the pump average power, R is the repetition rate of the laser (5 kHz),

E_{pump} is the pump energy and $A_{\text{laser}} = \pi D^2/4$ is the size of the focused pump beam on the sample with a diameter D . The absorption coefficient α of bilayer MoS₂ was determined by convolving the reflectivity spectra and the laser profile. We assume all of the absorbed photons form excitons. We note that these fluences correspond to hybrid exciton densities ($< 10^{11} \text{ cm}^{-2}$) well below the exciton Mott transition ($\sim 10^{12} \text{ cm}^{-2}$).

Estimate of polariton density

To estimate the polariton density n_{pol} presented in Fig. 4, we calculated the injected photon density based on the pump parameters and accounted for the coupling efficiency into the polariton modes. The injected polariton density during the pulse is estimated by:

$$n_{\text{pol}} = \frac{P\alpha}{CRA_{\text{laser}}E_{\text{pump}}}$$

Where C is the photonic fraction of the polariton states, this estimation allows us to correlate the observed energy blueshifts directly with the density of quasiparticles in the microcavity. It is important to note that our calculation assumes a unitary conversion efficiency from the absorbed pump photons (resonant with the B exciton) to the lower polariton reservoir. In practice, non-radiative scattering channels and relaxation bottlenecks likely result in a conversion efficiency below 100%. Consequently, our estimated polariton density represents an upper bound. Since the interaction strength is derived as $g_{\text{LP}} = \Delta E/n_{\text{pol}}$, any overestimation of the density implies that our reported g_{LP} values represent conservative lower bounds of the intrinsic nonlinearity, and the actual interaction strength may be even larger.

Estimate the dipolar interaction strengths.

Based on a parallel-plate model⁵⁶, the dipolar-dipolar interaction strength is given by $g_{\text{dd}} = e p_{\text{eff}} / \epsilon_0 \epsilon_{\text{eff}}$, where p_{eff} is the dipole moment of IE, which can be acquired from the Stark shift of IE and estimated to be 0.40-0.48 $e\cdot\text{nm}$ (see Supplementary Note 3). Theoretically, the effective permittivity is expected to lie close to the geometric mean of the heterostructure layers ($\epsilon_{\text{eff}} \approx \sqrt{\epsilon_{\text{TMD}}\epsilon_{\text{hbn}}} = 4.94$), thereby leading to an estimated dipolar interaction strength of $g_{\text{dd}} \approx 1.8 \text{ } \mu\text{eV}\cdot\mu\text{m}^2$.

Data availability

The data that support the findings of this study are available from the corresponding authors upon reasonable request.

Acknowledgments

Q. X. gratefully acknowledges funding support from the National Key Research and Development Program of China (Grant No. 2022YFA1204700), and funding support from National Natural Science Foundation of China (Grant No. W2541001, 12434011). K.W. and T.T. acknowledge support from the JSPS KAKENHI (Grant Numbers 21H05233 and 23H02052), the CREST (JPMJCR24A5), JST and World Premier International Research Center Initiative (WPI), MEXT, Japan. This work has been supported in part by the New Cornerstone Science Foundation.

Author contributions

Q.X. supervised the whole project. B.X. and Q.X. conceived the idea of the research. B.X. fabricated the devices with the help of Z.S. and G.W. Y.W. and B.X. established the optical paths. B.X. performed the steady and transient spectral measurements with the help of Y.W. B.X., G.W., and Y.W. analyzed the data with the guidance of Q.X., Z.S., and T.C.H.L. B.X. and Y.W. co-wrote the manuscript with contributions from all authors.

Competing interests

The authors declare no competing interests.

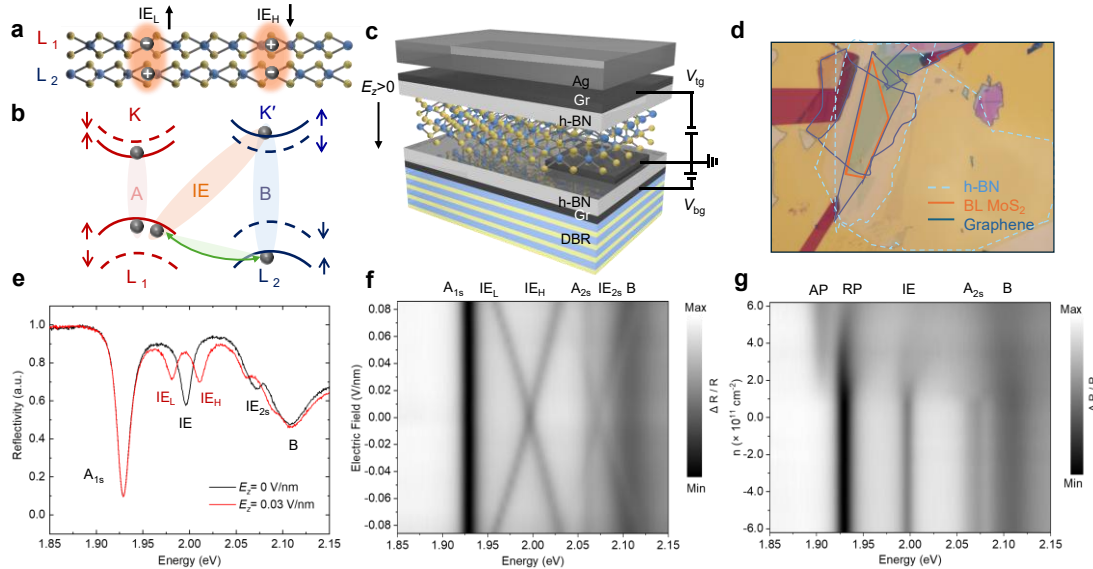


Fig. 1 | Dual-gated MoS₂ bilayer device and intrinsic optical characteristics at 9 K. **a**, Atomic structure and the spatial charge distribution of IEs in bilayer MoS₂. The top and bottom layers are labelled as L₁ and L₂, respectively. **b**, Band alignment of 2H-stacked bilayer MoS₂ at the K point under zero electric field, illustrating the optical transitions for the intralayer A and B excitons, and the hybrid IE. Hole tunneling (green arrow) between layers mediates the hybridization between the IE and the B exciton. Spin states are indicated by arrows. **c**, Device schematic showing the hBN-encapsulated bilayer MoS₂ heterostructure with top/bottom graphene gates atop a DBR mirror, sealed by a Ag top mirror. **d**, Optical micrograph of the device before top Ag mirror transfer. The bilayer MoS₂ (orange outline), hBN (blue outline), and graphene gates (grey outline) are indicated. Scale bar: 20 μ m. **e**, Reflectivity contrast spectra under $E_z = 0$ V/nm (black curve) showing A exciton, IE, and B exciton resonances, and under $E_z = 0.03$ V/nm (red curve) showing the Stark splitting of the IE resonance into IE_L and IE_H. **f**, False-color mapping of the reflectivity contrast spectra versus the applied electric field, demonstrating the colossal Stark splitting of the IE resonance, while intralayer excitons remain relatively field-independent. **g**, Doping-dependent reflectance spectra at zero electric field. Under electron doping ($n > 0$), the spectral weight of the A exciton shifts to the attractive polaron (AP, or trion) and repulsive polaron (RP) branches, while the IE resonance is quenched. In contrast, under hole doping ($n < 0$), both the A exciton and IE maintain robust oscillator strength.

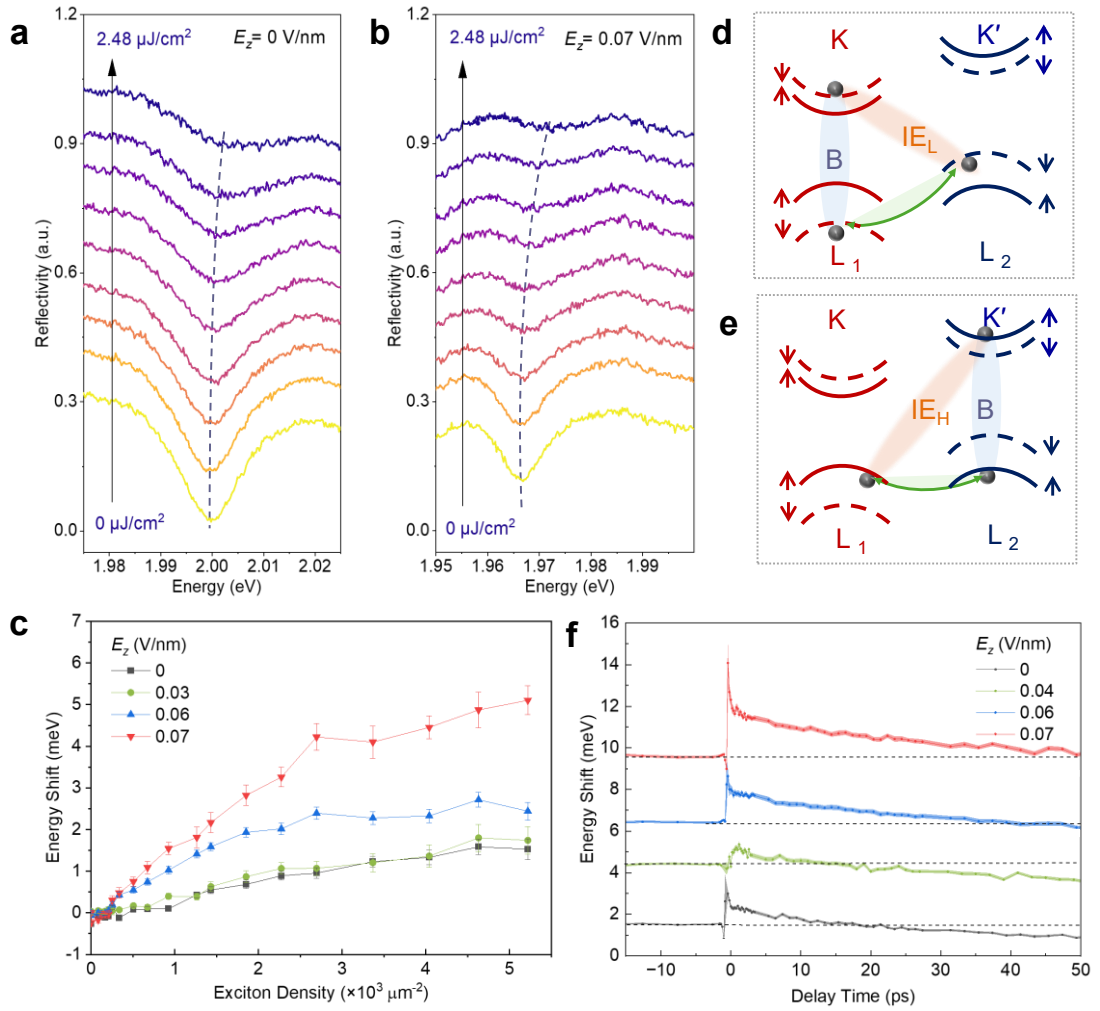


Fig. 2 | Electrically tunable exciton nonlinearity and dynamics in bilayer MoS₂. **a,b,** Pump-fluence-dependent transient reflectance spectra of IE (a) and IE_L (b) resonances at a fixed delay of 200 fs for $E_z = 0 \text{ V/nm}$ and $E_z = 0.07 \text{ V/nm}$, respectively. Dashed lines trace the energy blueshift with increasing excitation density. The error bars represent the uncertainty of the Lorentzian fit. **c,** Extracted energy blueshift of the IE_L resonance as a function of exciton density for different electric fields. **d,e,** Schematic illustration of the hybridization mechanism under a finite electric field. The field-induced energy offset suppresses hole tunneling rate J for the IE_L branch in (d) while enhancing it for the IE_H branch in (e), thereby tuning their interlayer character and interaction strength. **f,** Temporal dynamics of the IE_L blueshift at different electric fields, showing a significant prolongation of the nonlinear interaction lifetime as the field increases.

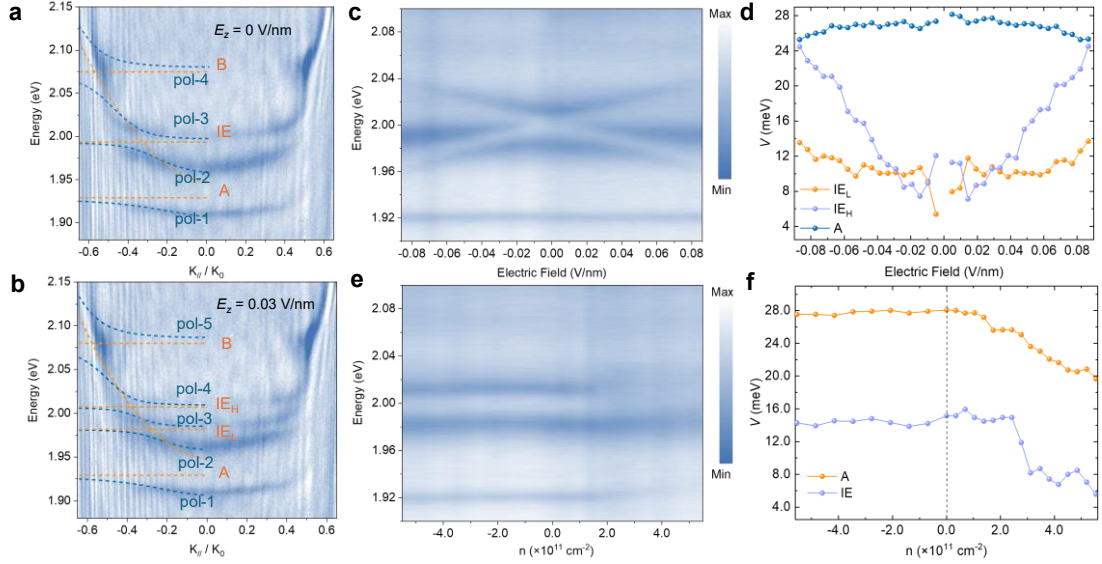


Fig. 3 | Electrically reconfigurable strong coupling and polariton dispersion in a dual-gated MoS₂ microcavity. **a,b,** Angle-resolved reflectivity spectra at (a) $E_z = 0$ V/nm and (b) $E_z = 0.03$ V/nm, respectively. Dashed lines are guides to the eye for the polariton eigenvalues (orange) and the cavity modes (blue) obtained from fitting using the coupled oscillator model. **c,** False-color mapping of reflectivity spectra extracted at $k_{\parallel}/k_0 = 0.33$ as a function of electric field. **d,** Extracted coupling strengths (half of the Rabi splitting) for the A exciton (blue), IE_L branch (orange), and IE_H branch (purple) as a function of the electric field, derived from the coupled oscillator model. **e,** False-color mapping of reflectivity spectra extracted at $k_{\parallel}/k_0 = 0.33$ as a function of doping density. **f,** Extracted coupling strength of the IE and A exciton resonance as a function of doping density, demonstrating a clear quenching of the strong coupling under electron doping.

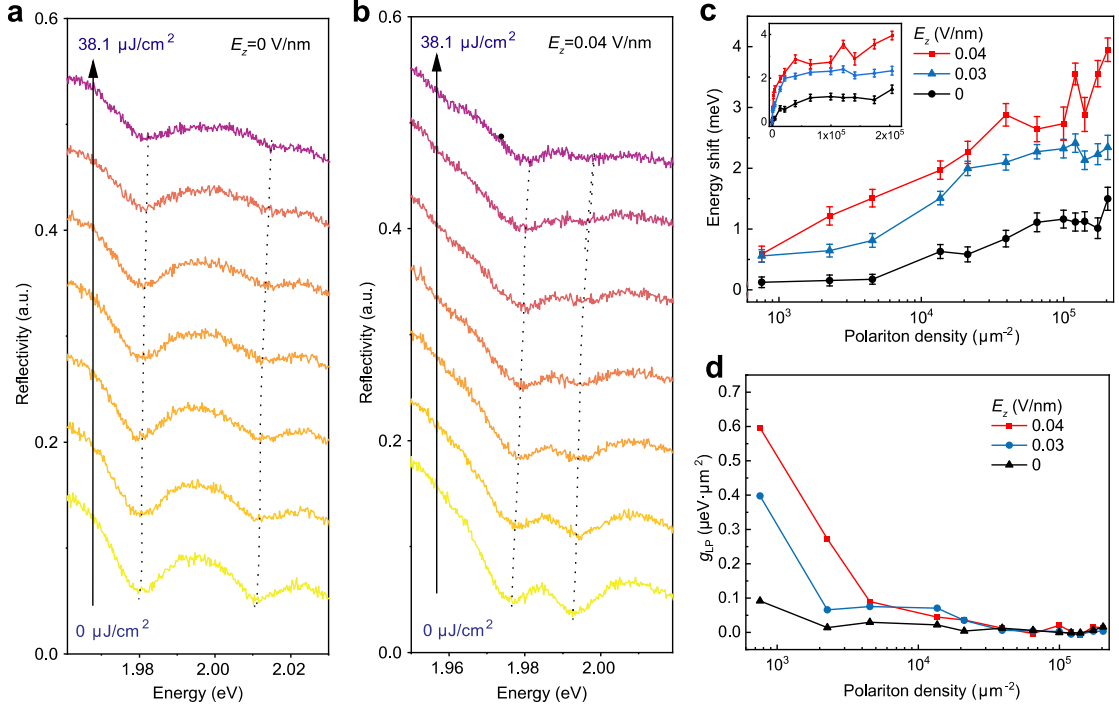


Fig. 4 | Electrical tuning of polariton nonlinearities. **a,b**, Resonant reflectivity spectra of the lower and upper polariton branches (LPB and UPB) of IE_L at zero-detuning for (a) $E_z = 0$ V/nm and (b) $E_z = 0.04$ V/nm, as a function of increasing pump-induced polariton density. Dashed lines are guides for the eyes, highlighting the density-dependent blueshift. **c**, Extracted energy shift of the IE_L -associated LPB at zero-detuning wavevector versus polariton density for different applied electric fields. The main panel utilizes a logarithmic x-axis to illustrate the nonlinear behavior over a wide density range, whereas the inset displays the data on a linear scale to clearly visualize the steep initial rise corresponding to the giant interaction strength. The error bars represent the uncertainty of the Lorentzian fit. **d**, Nonlinear interaction strength g_{LP} as a function of polariton density. The low density interaction strength at $E_z = 0.04$ V/nm is almost seven-fold larger than that at $E_z = 0$ V/nm.